

Article

# Influence of the Ni Catalyst on the Properties of the Si-C Composite Material for LIB Anodes

Darina A. Lozhkina <sup>1</sup>, Vladimir P. Ulin <sup>1</sup>, Mikhail E. Kompan <sup>1</sup>, Aleksander M. Rumyantsev <sup>1</sup>, Irina S. Kondrashkova <sup>2</sup>, Andrei A. Krasilin <sup>1</sup>  and Ekaterina V. Astrova <sup>1,\*</sup>

<sup>1</sup> Ioffe Institute, Politekhnicheskaya 26, Saint-Petersburg 194021, Russia

<sup>2</sup> Saint-Peterburg State Institute of Technology, Technical University, Moskovsky pr. 26, Saint-Petersburg 190013, Russia

\* Correspondence: east@mail.ioffe.ru

**Abstract:** The subject of this study was Si-C composites for lithium-ion battery (LIB) anodes obtained by carbonization of nanodispersed silicon with carbon monofluoride. To determine the possibility of increasing the degree of graphitization of nanodispersed carbon forming shells around the silicon particles at lower temperatures, nickel in the form of an alcoholic solution of  $\text{Ni}(\text{NO}_3)_2$  was introduced as a catalyst into the pellets of the resulting composite. The XRD, Raman scattering and EDS methods were used to investigate changes both in the phase and elemental composition of materials resulting from the annealing of the Ni-containing Si-C composite over the temperature range of 500–1100 °C. It was found for the first time that nickel silicides that emerged during the annealing became catalysts and, at the same time, intermediate products, of cubic silicon carbide ( $\beta\text{-SiC}$ ) synthesis, which reduced its temperature formation from ~1100 °C to ~800 °C. The same compounds had a catalytic effect on the carbon atom association, leading to an increase in the degree of its graphitization. The influence of changing the composition of the investigated material on the electrochemical characteristics of the obtained negative LIB electrodes was traced.



**Citation:** Lozhkina, D.A.; Ulin, V.P.; Kompan, M.E.; Rumyantsev, A.M.; Kondrashkova, I.S.; Krasilin, A.A.; Astrova, E.V. Influence of the Ni Catalyst on the Properties of the Si-C Composite Material for LIB Anodes. *Batteries* **2022**, *8*, 102. <https://doi.org/10.3390/batteries8080102>

Academic Editors: Tatiana L. Kulova and Alexander Skundin

Received: 29 July 2022

Accepted: 18 August 2022

Published: 21 August 2022

**Publisher's Note:** MDPI stays neutral with regard to jurisdictional claims in published maps and institutional affiliations.



**Copyright:** © 2022 by the authors. Licensee MDPI, Basel, Switzerland. This article is an open access article distributed under the terms and conditions of the Creative Commons Attribution (CC BY) license (<https://creativecommons.org/licenses/by/4.0/>).

## 1. Introduction

Search of electrode materials capable of increasing the energy capacity of LIBs is an actual topic of contemporary research. Silicon, a material with extremely high specific gravimetric capacity, is considered to be the most promising for fabrication of LIB negative electrodes. Problems that arise in the practical application of Si [1–7] are generally solved by using it in the form of nanosized particles and forming silicon-carbon composites [4]. Coating the silicon particle surface with a layer of carbon makes it possible to increase the capacity and improve rate capability of the electrodes by reducing their electrical resistance. In addition, an increase in the Coulombic efficiency and cyclic life of the electrode is achieved due to the shift of the solid electrolyte interphase (SEI) formation region to the outer carbon shell of silicon particles.

Recently, we have proposed a new technology of Si-C nanocomposite formation by a low temperature (~600 °C) reduction of carbon by silicon from its fluorides. A powder of solid-phase carbon monofluoride mixed with a powder of nanodispersed silicon was used as a distributed source of gaseous carbon fluorides [8–10]. A shell of low ordered carbon is formed around Si nanoparticles after annealing of the mixture. This carbon shell is conjugated with other shells of neighboring particles into a continuous conductive network throughout the entire volume of the resulting composite. Since the reduction of carbon by silicon proceeded with the participation of gaseous compounds and required the removal of the gaseous byproduct ( $\text{SiF}_4$ ), the resulting carbon material gained a well-developed loose porous structure. Such a structure provides efficient accommodation for

Si particles during cyclic volume changes in the processes of lithiation–delithiation of LIB anodes. At the same time, the high dispersion of the carbon component of the composites reduces its electrical conductivity, and the large specific surface area of carbon particles causes significant irreversible losses during the formation of SEI. Therefore, the problem of increasing the degree of graphitization of low ordered carbon in such composites becomes topical [11]. It is known that graphitization of amorphous carbon occurs at very high temperatures  $>1700\text{ }^{\circ}\text{C}$  [12]. These temperatures are unacceptable in the case of Si-C composites due to the formation of cubic silicon carbide  $\beta\text{-SiC}$  at  $T\sim1100\text{ }^{\circ}\text{C}$ . The forming carbide does not demonstrate a noticeable capacity with respect to Li [13].

In the present work, we attempted to order the structure of the carbon coating, while avoiding its transformation into Si-C, by lowering the carbon graphitization temperature in the presence of catalysts. In contact with transition metals such as Fe, Co and Ni, the graphitization temperature of amorphous carbon decreases below  $1000\text{ }^{\circ}\text{C}$  [14–17]. Here we studied the influence of Ni on the composition, structure and electrochemical performance of Si-C composites heat treated in the  $500\text{--}1100\text{ }^{\circ}\text{C}$  temperature range.

## 2. Materials and Methods

The synthesis of composites was carried out in two stages. The precursors for this process were Si nanopowder (Hongwu Nanometer, China) with an average particle size of 40 nm and fluorocarbon powder  $\text{CF}_x$ , where  $x = 0.82$  (Halo Polymer, Russia). Powders taken in the weight ratio 30 wt.% Si + 70 wt.%  $\text{CF}_{0.82}$  were thoroughly mixed and ground in an agate mortar. Pellets 10 mm in diameter and  $\sim650\text{ }\mu\text{m}$  thick were prepared from the resulting mixture by cold dry compaction under a pressure of 180 MPa. The samples were annealed in a quasi-closed volume of graphite cassettes. The cassettes were placed in a muffle furnace with a quartz tube purged with high-purity argon (99.998%) and were heated to  $400\text{ }^{\circ}\text{C}$ . Then the temperature was increased at a rate of  $3.3\text{ }^{\circ}\text{C}/\text{min}$  up to  $800\text{ }^{\circ}\text{C}$  and maintained at this level for 20 min, followed by slow cooling in an Ar atmosphere down to  $500\text{ }^{\circ}\text{C}$ . The composite samples obtained as a result of such annealing are referred to in the text as “as carbonized”. At the second stage, part of the annealed pellets was saturated by a 6 wt.%  $(\text{Ni}(\text{NO}_3)_2 \cdot 6\text{H}_2\text{O})$  alcohol solution and dried at  $60\text{ }^{\circ}\text{C}$  until the solvent and bound water were completely removed. The saturation was carried out so that the final increase in the pellet weight was  $\sim60$  wt.%. After that, the Ni-containing and control pellets were loaded into a tube filled with Ar and heated to  $200\text{ }^{\circ}\text{C}$ , followed by an increase in temperature at a rate of  $3.3\text{ }^{\circ}\text{C}/\text{min}$  to the target temperature in the  $500\text{--}1100\text{ }^{\circ}\text{C}$  range, maintained for 2 h, and slowly unloaded for 10 min.

Scanning electron microscopy (SEM) and energy dispersive X-ray spectroscopy (EDS) of the obtained composites were carried out using an FEI Quanta 200 scanning electron microscope (FEI company, Hillsboro, OR, USA). X-ray diffraction (XRD) study was carried out using a Rigaku Corporation SmartLab 3 diffractometer (Rigaku Corporation, Japan) equipped with a copper anode and an Ni-filter ( $\lambda = 0.1542\text{ nm}$ ). Diffraction patterns were recorded by scanning at  $5\text{--}80^{\circ}$  intervals  $2\theta$  with  $0.01^{\circ}$  step. The phase analysis was created by using the ICDD PDF-2 database. Peak fitting was carried out using the Fityk program [18]. Reflexes suitable for analysis were in the  $2\theta$  range of  $25\text{--}65^{\circ}$  angles. The reflexes were approximated by the Pearson 7 function. Crystallite sizes were calculated using the Scherrer equation:

$$d = K\lambda/(\beta \cos \theta) \quad (1)$$

where  $d$ —crystallite size, nm;  $\lambda$ —radiation wavelength, nm;  $\theta$ —scattering angle, rad;  $\beta$ —width of the reflex at half its maximum intensity, rad;  $K = 1$ . The calculation error did not exceed 10%.

The analysis of structural changes in the low ordered carbon shell of Si-C composites was carried out on the basis of the obtained Raman spectra. Raman scattering experiments were carried out on a HORIBA-JOBIN-YVON MRS 320 modular micro-Raman spectrometer (Horiba Scientific, Kyoto, Japan) equipped with an OLIMPUS BX41 microscope (Kyoto, Olympus, Japan). For excitation, a He-Ne laser with a wavelength of 632.81 nm was used.

The radiation power did not exceed 2 mW. The scattered light was separated from the background of the excitation light by a step-filter and was recorded by a CCD receiver. The experiments were carried out at room temperature. To fit the spectra, the Fityk program was used.

Thermodynamic calculations were made using the IVTANTERMO program package version 30-3 to estimate the temperatures of the start of the decomposition reactions of nickel nitrate and the interaction of nickel oxide with carbon [19].

For the fabrication of electrodes from the obtained pellets, their thickness was reduced by grinding to 100  $\mu\text{m}$ . The mass of the samples was 1–3 mg after grinding. After that, the samples were glued onto copper foil using a suspension based on polyvinylidene fluoride (PVDF), highly split graphite and NMP (N-methylpyrrolidone).

The electrochemical measurements of the samples were performed with coin cells CR2032 using lithium metal as the counter electrode. The electrolyte was Tinci TC-E918 (Guangzhou Tinci Materials Technology Co, LTD, GuangZhou, China), which was a 1 M solution of LiPF6 in a mixture of EC/PC/DEC/EMC/PA (ethylene carbonate, propylene carbonate, diethyl carbonate, ethyl methyl carbonate, propyl acetate). The cells were galvanostatically charged and discharged at various current densities ranging between 10 mV and 2 V (vs. Li/Li<sup>+</sup>) on the Neware CT 3008 W-5 V 10 mA testing system (Neware, Hong Kong, China).

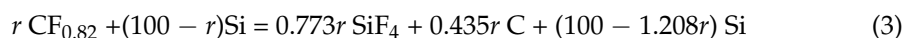
### 3. Results and Discussion

#### 3.1. Formation of Composites

Formation of the initial Si-C nanocomposites begins with the disproportionation of solid-state fluorocarbon and the release into the gas phase of lighter fluorocarbon molecules. These molecules interact with the surface of Si particles with formation of carbon and gaseous SiF<sub>4</sub>. The resulting carbon forms a layer of gas-permeable amorphous material around silicon particles. However, in the amorphous carbon the association of atoms immediately begins to develop, leading to the emergence of fragments consisting of graphene networks from sp<sup>2</sup>-hybridized atoms, and their mutual ordering occurs. This process is caused by the tendency of carbon to go into the most thermodynamically stable state at normal pressure. The size and density of the graphite-like nanoparticles depend on initial density of carbon atoms reduced on the silicon surface, temperature, and duration of the heat treatment. In addition, a noticeable amount of free carbon (~20% of the total mass of carbon) remains in the solid phase after the decomposition of non-stoichiometric carbon monofluoride. This carbon retains residual fluorine and, probably, has a higher degree of graphitization compared to carbon formed during the chemical interaction of gaseous fluorides with silicon [9,10]. The overall reaction describing these processes can be represented as:



Under the condition of a super stoichiometric excess of silicon necessary to obtain a composite, the mass balance of substances participating in Reaction (1) for x = 0.82 can be written as follows:

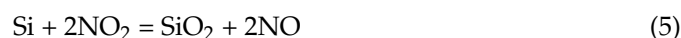


where r is the content of fluorocarbon in weight percent.

We used r = 70% for the composition of the initial mixture, then the concentration of C and Si in the resulting composite should be 66 wt.% (82 at.%) and 34 wt.% (18 at.%), respectively, according to Equation (3). The correctness of this estimation was confirmed by the actual reduction in the weight of the pellets during annealing (54.8%) in comparison with the calculated value (54.1%).

Nickel oxide formation and oxidation of silicon surface by released oxygen and nitrogen dioxide are the first chemical processes developing at increasing temperature after introduction of nickel nitrate into the composite. (According to thermodynamic evaluation,

decomposition of nickel nitrate should start at  $T \sim 300$  °C). Nickel oxide can be reduced by both carbon and silicon to metallic nickel by further increasing the temperature in an inert atmosphere. Then nickel interacts with silicon to form the corresponding silicides. It is estimated that the reduction of nickel by carbon can start at  $T \sim 500$  °C. The interaction of passivating  $\text{SiO}_2$  films on the surface of silicon particles with  $\text{NiO}$  to form nickel silicate may be a side process that contributes to the destruction of the  $\text{SiO}_2$  films. Nickel can be reduced with carbon or silicon from its silicate at higher temperatures. The initial chemical processes occurring during annealing of Ni-containing Si-C composites can be roughly represented by the following reactions:



It is not difficult to calculate the ratio of atomic concentrations of the main elements (Ni, Si and C) involved in the chemical transformations averaged over the volume of the annealed material. We found that the relative amount of elements is the following: Ni/Si~0.27; Ni/C~0.06, mole fraction of Ni relative to the total amount of Si and C~8.7 at.%.

### 3.2. Scanning Electron Microscopy

The SEM image in Figure 1 demonstrates heterogeneous structure of a sample annealed at 1100 °C.

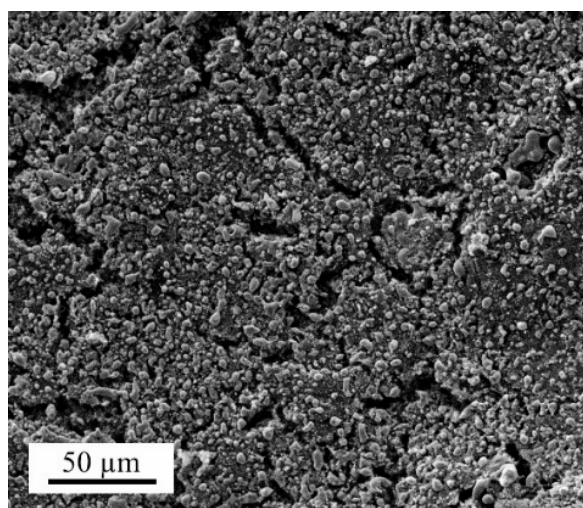


**Figure 1.** SEM image of the surface of a sample with Ni annealed at 1100 °C.

EDS showed the following values for the averaged composition of particles coming to the surface: 32 at.% Ni; 18.8 at.% Si; 44.9 at.% C; 0.6 at.% F; 3.5 at.% O. We registered a significant excess of the nickel content in the surface layer of the sintered composite in relation to other elements as compared with the calculated values. This observation can be explained by the fact that the nickel nitrate was initially concentrated in their near-surface layer, as a result of drying the pellets soaked in a salt solution. This spatial distribution of salt is the

result of slow evaporation of the solvent from the porous material. The salt begins to crystallize on the outer open surface of the sample as the solvent evaporates. Diffusion flows emerge in the pore channels of both solvent and dissolved substance from the volume to the open surface if a wetting layer exists. The wetting layer is a supersaturated solution on the surface of growing salt crystals. We can also assume that after annealing the main nickel-containing phase on its surface was nickel silicide  $\text{Ni}_2\text{Si}$  based on the ratio  $\text{Ni}/\text{Si} = 1.7$  for the surface layer of the pellet. The detected elemental composition of the surface layer of the pellets remained practically the same for all annealing temperatures starting from  $800\text{ }^\circ\text{C}$ . Homogeneous distribution of elements at their practically unchanged ratio (Figure 2) was observed in the volume of samples, regardless of the annealing temperature. According to EDS data, the total Ni content in the volume of pellets was  $\sim 5.5$  at.%, Si~ $10.8$  at.%, C~ $73.4$  at.%. The obtained nickel content satisfactorily agrees with the initial estimation of the total nickel concentration in the sample, taking into account the detected nickel enrichment of the near-surface layer of the annealed pellets. In addition, O and F were detected in the samples, the total content of which decreased when the annealing temperature rose to  $1100\text{ }^\circ\text{C}$  from 10 to 5.7 at.%, and from 1 to 0.5 at.%, respectively. The presence of fluorine and oxygen can be explained by the above reactions and incomplete disproportionation of carbon monofluoride during the formation of the initial Si-C composite.

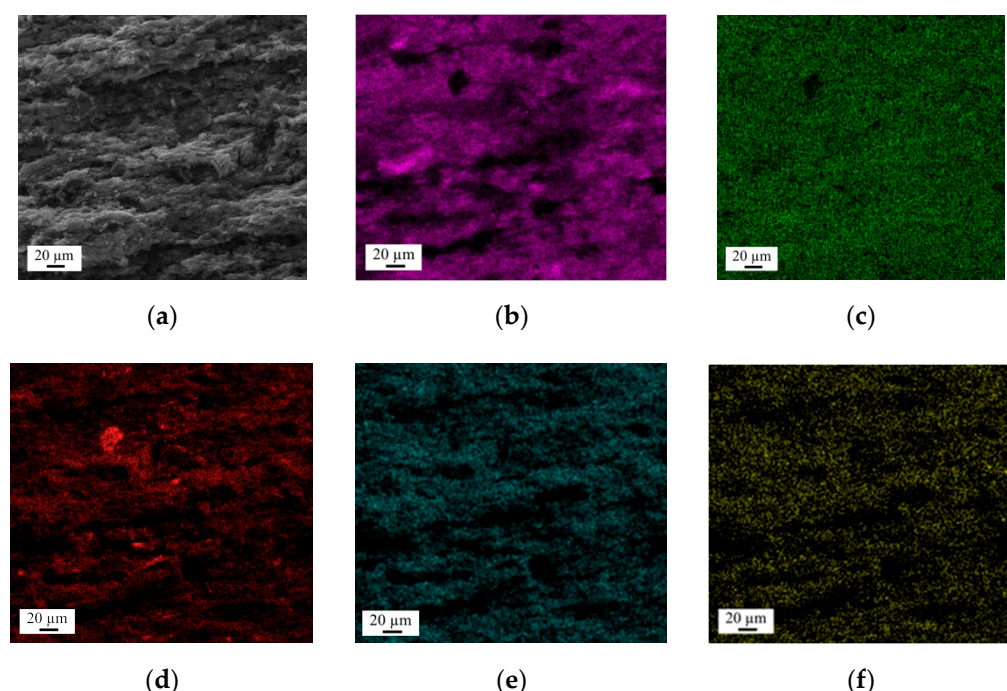


**Figure 2.** Cross-section of the sample with Ni annealed at  $800\text{ }^\circ\text{C}$ : (a) SEM image; (b–f) element distribution maps. (b) Si; (c) Ni; (d) C; (e) O; (f) F.

### 3.3. X-ray Diffraction

Figure 3 shows diffraction patterns of pellets that were heat-treated at different temperatures, with Ni and control ones without Ni. For a correct comparison of the peaks shown in Figures 3–5 their integral intensities were normalized by dividing by the sample mass,  $I/m$ .

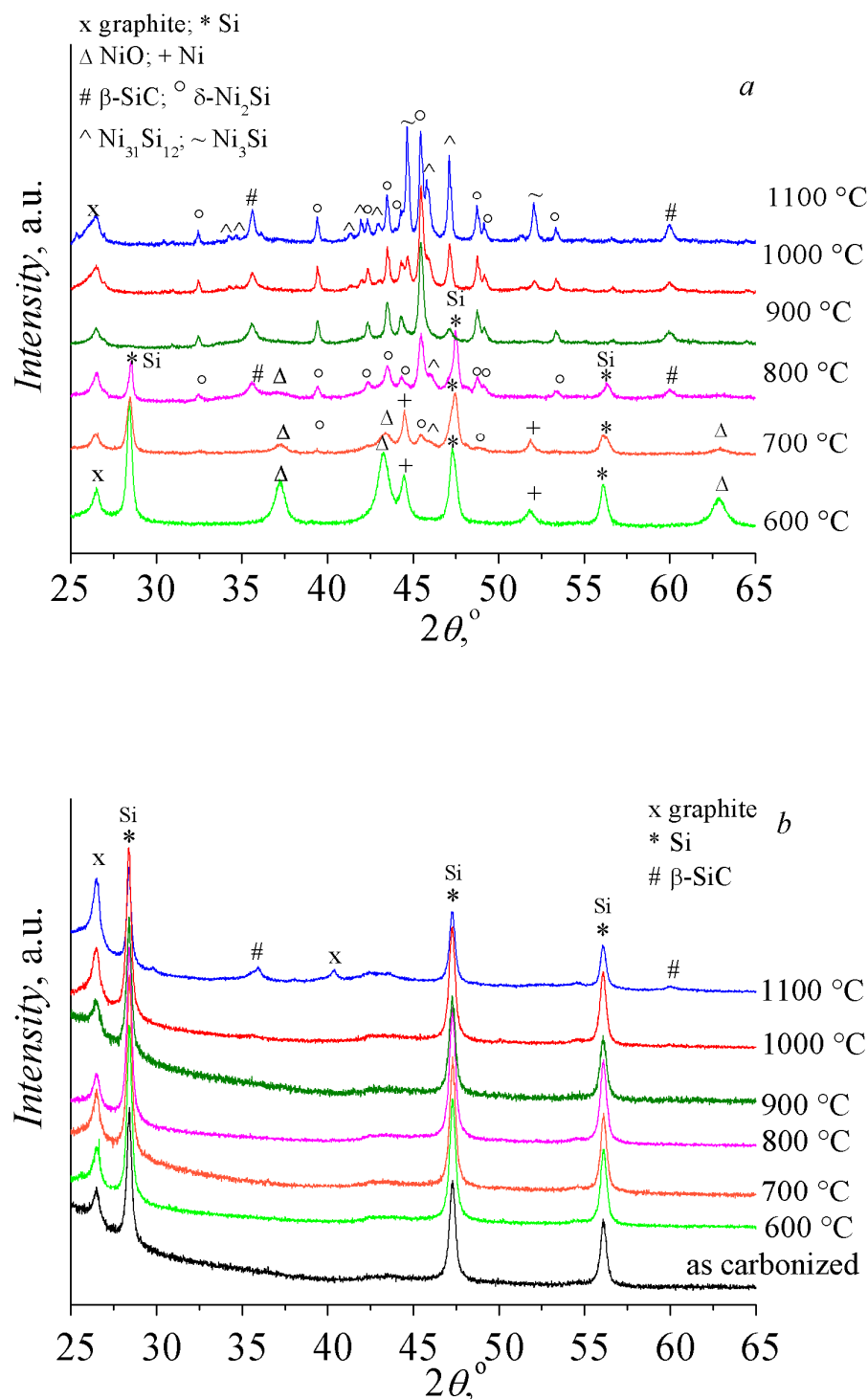


**Figure 3.** XRD patterns of samples annealed at different temperatures: (a) composites with Ni, (b) control without Ni.

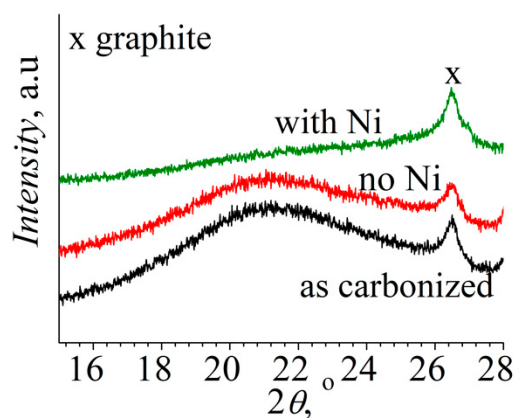


**Figure 4.** Reflexes in the  $2\theta$  range of  $15\text{--}28^\circ$  angles for as carbonized sample, control and Ni-containing samples annealed at  $900\text{ }^\circ\text{C}$ .

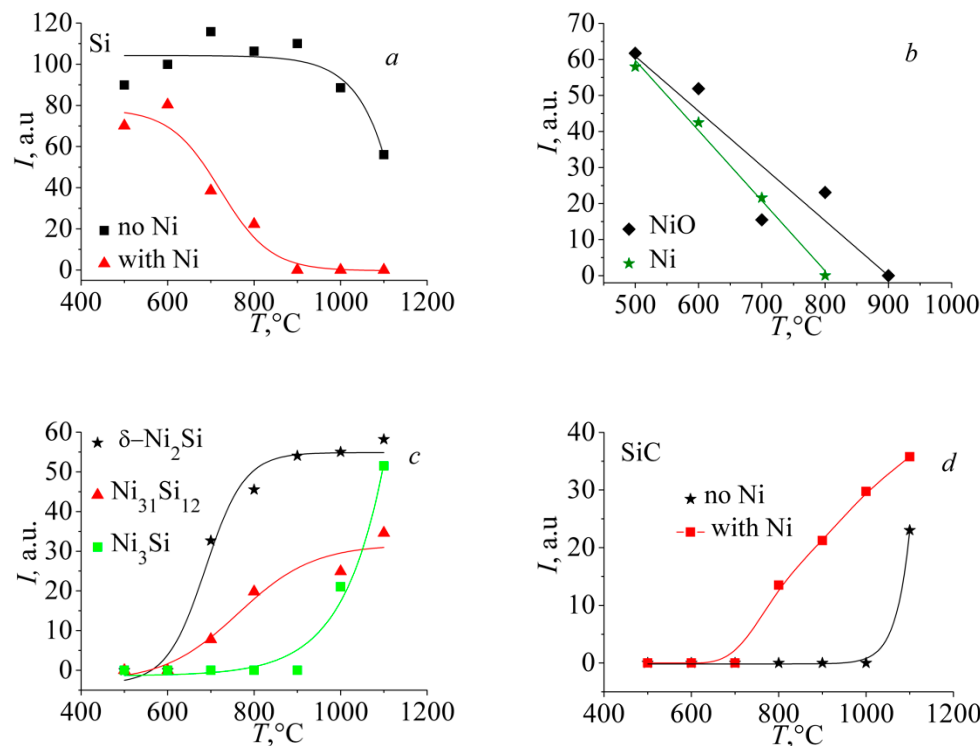


**Figure 5.** Change in the normalized value of the integral intensity of XRD peaks  $I/m$  for a single reflex of each phase, registered in samples with Ni: (a) Si  $2\theta = 28.4^\circ$ ; (b) NiO  $2\theta = 37.3^\circ$ ; Ni  $2\theta = 44.5^\circ$ ; (c) –  $\delta\text{-Ni}_2\text{Si}$   $2\theta = 45.5^\circ$ ;  $\text{Ni}_{31}\text{Si}_{12}$   $2\theta = 46^\circ$ ;  $\text{Ni}_3\text{Si}$   $2\theta = 44.7^\circ$ ; (d) – SiC  $2\theta = 35.6^\circ$ .

The XRD patterns (Figure 3a) show that the reduction of nickel oxide by carbon began at  $500\text{ }^\circ\text{C}$  and finished above  $800\text{ }^\circ\text{C}$  (the XRD patterns for  $500$  and  $600\text{ }^\circ\text{C}$  are identical, therefore only the pattern for  $600\text{ }^\circ\text{C}$  is shown). The resulting nickel was already completely transformed into the nickel silicide form  $\delta\text{-Ni}_2\text{Si}$  (PDF 48-1339) by this temperature. A further increase in the annealing temperature to  $1000\text{ }^\circ\text{C}$  resulted in new crystalline nickel silicide phases  $\text{Ni}_{31}\text{Si}_{12}$  (PDF 24-524) and  $\text{Ni}_3\text{Si}$  (PDF 3-1048) containing more nickel. This seemed surprising, taking into account the significant excess of silicon over nickel in the system. It is worth noting that the formation of silicon carbide  $\beta\text{-SiC}$  (PDF 2-1050) occurred as early as  $800\text{ }^\circ\text{C}$ . Whereas in the control Si-C composites annealed at the same temperature as composites containing nickel, that  $\beta\text{-SiC}$  was formed at higher temperature  $1100\text{ }^\circ\text{C}$  (Figure 3b). A comparison of XRD patterns of samples with and without Ni formed at  $900\text{ }^\circ\text{C}$  is presented in Figure 4. It should be noted, that XRD patterns of control and as

carbonized samples showed a halo in the  $15\text{--}25^\circ$  region, which decreased in the nickel-containing samples. It can be assumed that this halo is caused by amorphous carbon [20]. The peaks at  $2\theta = 26^\circ$  and  $40^\circ$  (both seen in Figure 3b) are probably due to graphite-like carbon (PDF 12-212), which emerged initially due to disproportionation of  $\text{CF}_x$  and due to subsequently ordering of the carbon structure.

Estimation of crystallite size of chemically stable phases of nickel silicides and silicon carbide formed during the annealing show that along with the total phase content (Figure 5) the particle size increases as the annealing temperature grows (Figure 6). We should especially note the unexpected tendency for a successive increase in the relative concentration of the silicide phases with a higher nickel content ( $\text{Ni}_2\text{Si} \rightarrow \text{Ni}_{31}\text{Si}_{12} \rightarrow \text{Ni}_3\text{Si}$ ) as the annealing temperature increases, despite the significant excess of silicon over nickel in the initial material. This behavior can only be explained by the catalytic effect of nickel atoms on carbon atoms, which results in the formation of silicon carbide. This process occurs, indirectly, through nickel silicides  $\text{Ni}_2\text{Si}$  and  $\text{Ni}_{31}\text{Si}_{12}$ . That is, in the temperature range, when the presence of direct contact of carbon with silicon particles does not yet lead to the formation of  $\text{SiC}$ , the contact of previously formed  $\text{Ni}_2\text{Si}$  particles with carbon led to the formation of silicon carbide:

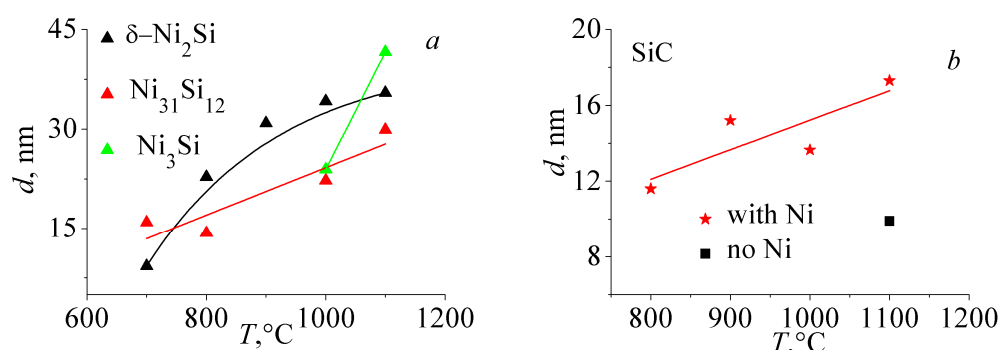


**Figure 6.** Temperature dependence of crystallite size for phases: (a)  $\delta\text{-Ni}_2\text{Si}$ ;  $\text{Ni}_{31}\text{Si}_{12}$ ;  $\text{Ni}_3\text{Si}$ ; (b)  $\beta\text{-SiC}$ .

As long as the concentration of free silicon in the composite remained high enough, the resulting silicide with a higher nickel content was transferred back to the original one:

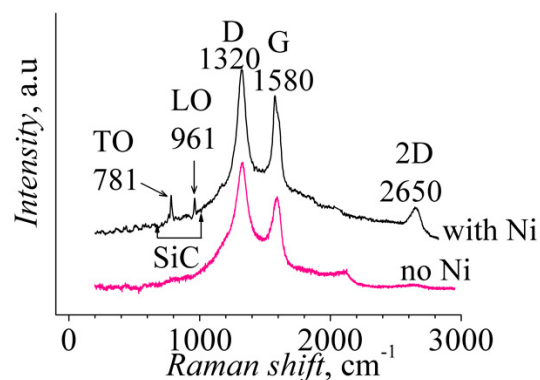


However, when free silicon had been exhausted to form  $\text{SiC}$ , there was rapid accumulation of silicide with maximum nickel content, which correlates with the data shown in Figure 5. Apparently, activation of carbon atoms occurs in the area of their contact with Ni-containing particles in the processes under consideration, as well as in the long-studied processes of graphitization of amorphous carbon in the presence of nickel, iron and other transition d-elements [14]. The reason for this effect should be sought in the exchange of valence electrons on the occupied orbitals of carbon atoms with the vacant d-orbitals of nickel atoms that are part of the silicides.

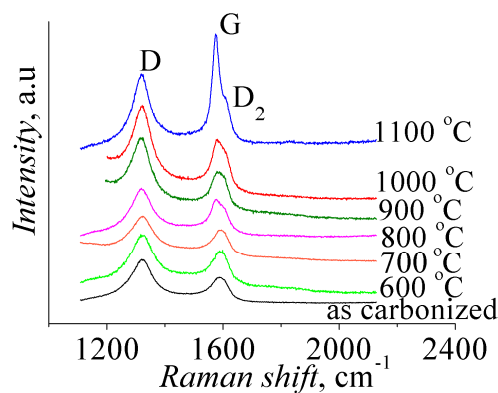
### 3.4. Raman Scattering

Figure 7 shows Raman spectra of the nickel-containing sample and the control sample annealed at  $T = 800\text{ }^\circ\text{C}$ . For the Ni-containing sample, silicon carbide peaks due to TO and LO phonons were observed. Fitting their contour using the Pearson 7A function showed that the maximum corresponds to frequencies  $782$  and  $961\text{ cm}^{-1}$ , and the FWHM widths are  $11$  and  $10\text{ cm}^{-1}$ , respectively. It should be noted that these frequencies are shifted to lower energies relative to the position of the peaks in bulk  $\beta\text{-SiC}$  ( $796$  and  $972\text{ cm}^{-1}$ ) [21],

which may be due either to stacking fault defects or to quantum confinement effects in nanoscale crystals that shift the characteristic frequencies of phonons [22]. Characteristic bands of nanocrystalline graphite [23,24] were observed throughout the temperature range for the samples with Ni and for the control samples. The first-order spectrum in the  $1000\text{--}1700\text{ cm}^{-1}$  range was represented by two peaks, D and G. In some samples the G peak had a high-energy shoulder  $D_2$  at frequency  $1615\text{ cm}^{-1}$  (Figure 8). The second-order spectrum detected a 2D peak at  $\approx 2650\text{ cm}^{-1}$ , often of small amplitude, and sometimes a D +  $D_2$  peak at  $2900\text{ cm}^{-1}$  was observed. Band G is associated with the valence vibrations of  $sp^2$ -hybridized carbon atoms in the plane of the graphene layer. D is due to vibrations of the aromatic rings as a whole. D mode is forbidden for perfect crystals of graphite and graphene and emerges when the lattice is disordered. According to the ratio of intensities of peaks D and G and their width, one can estimate the degree of graphitization of the carbon material.



**Figure 7.** Raman spectra of Ni-containing and control samples annealed at  $800\text{ }^\circ\text{C}$ .



**Figure 8.** First-order Raman spectra of carbon in samples with Ni heat-treated at different temperatures shown in the graph.

Figure 8 shows how the spectrum of first-order carbon modes changes depending on the annealing temperature. A narrowing of the D and G peaks and a change in their relative intensity is seen. Figure 9 shows the height ratio of peaks D and G. It can be seen that in the control samples, the change in the annealing temperature has no noticeable effect on the relative height of the D and G peaks, whereas in the nickel-containing samples, the  $H_D/H_G$  ratio decreases with the temperature increase.

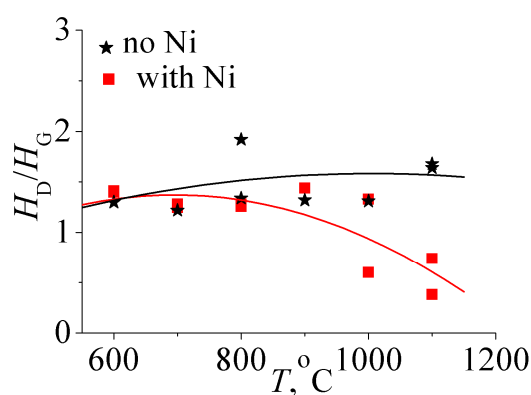


**Figure 9.** Temperature dependence of D and G peak height ratio  $H_D/H_G$  for nickel-containing and control samples.

The defectiveness of the graphite-like material can also be estimated from the width of the D and G bands measured at their half-height  $FWHM$ . The narrowing of these lines indicates a decrease in the number of structural defects [25]. The width of the G peak in the control samples practically does not change and the D peak width decreases only slightly as the temperature increases, while in the nickel-containing samples a narrowing of both peaks can be seen in Figure 10. In [26] it was shown that a decrease in the width of the G peak in nanocrystalline graphite is associated with an increase in the lateral size of graphite clusters  $L_a$ , which can be found from the equation

$$FWHM = 14 + 430/L_a \quad (13)$$

where  $FWHM$  in  $\text{cm}^{-1}$ ,  $L_a$  in nm.

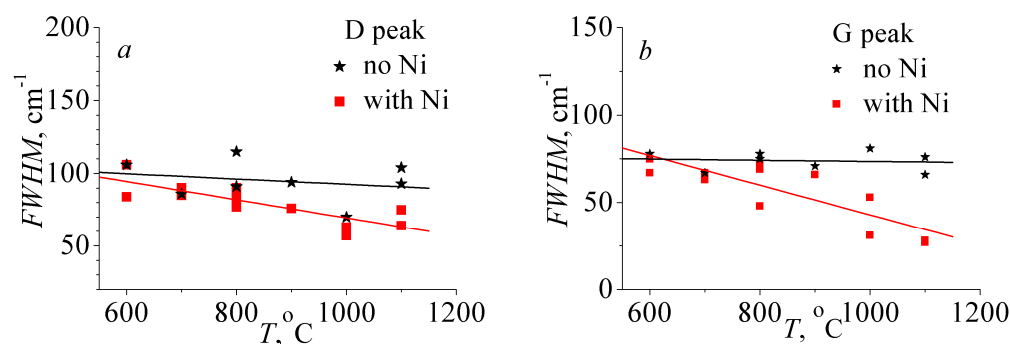


**Figure 10.** Peak width ( $FWHM$ ) as a function of heat treatment temperature for nickel-containing and control samples: (a) for D peak, (b) for G peak.

The calculation shows that an increase in the temperature of the heat treatment of nickel-containing samples from 600 to 1100 °C results in a 4-fold increase in  $L_a$  from 7 to 29 nm, while in the control samples it remains unchanged at 7 nm. Thus, analysis of Raman spectroscopy data indicates the catalytic effect of nickel, leading to a more effective graphitization of carbon during low-temperature annealing.

### 3.5. Electrochemical Characterization

The voltage profiles of the first cycle for samples with Ni and control (without Ni), as well as for as carbonized samples, are shown in Figure 11. In the case of control samples, the annealing temperature did not change the charge-discharge curves, as shown in Figure 11a. They remained practically the same as for the as carbonized sample.

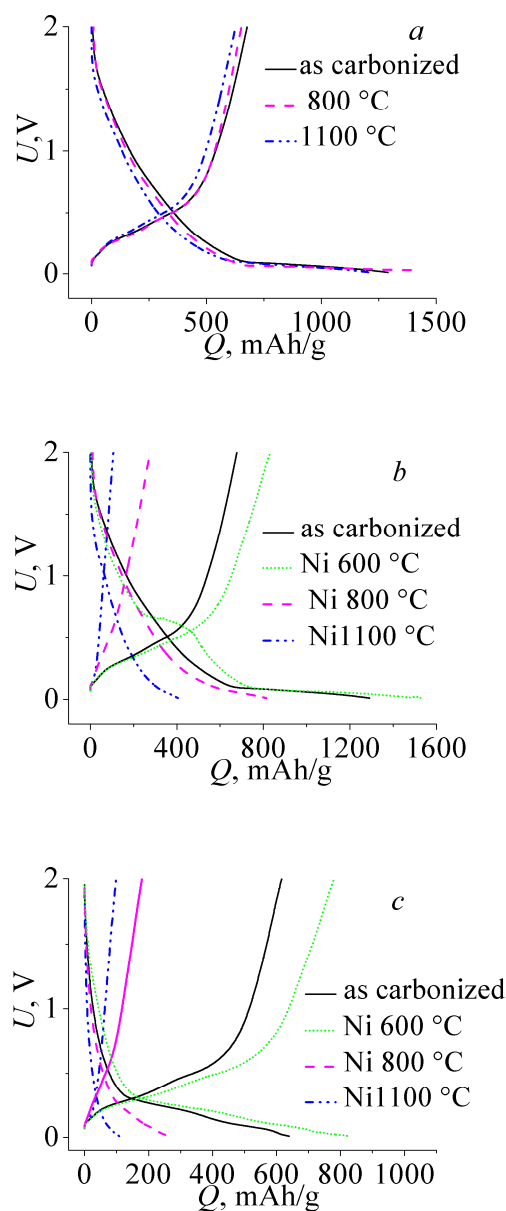


**Figure 11.** Voltage profiles of the first (**a,b**) and fifth (**c**) cycles for samples annealed at different temperatures.

In contrast to the control samples, the electrochemical performance of the nickel-containing samples strongly depends on the annealing temperature (Figure 11b,c). Annealing at 600 °C led to an increase in both the charge and discharge capacities of the electrodes compared to the capacity of the as carbonized electrode. A clearly pronounced plateau at a voltage of  $U = 0.6$  V can be seen on the voltage profile for the first lithiation of the sample annealed at 600 °C (Figure 11b). The plateau dropped out in subsequent cycles (Figure 11c). The presence of nickel oxide in the composition of the material explains the emergence of this region. As was shown in [27–29], the plateau at ~0.5 V is due to the reduction of NiO to Ni, accompanied by the formation of amorphous Li<sub>2</sub>O, and the electrolyte decomposition to form the SEI layer at the first lithiation



According to the same work, the reverse reaction of nickel oxidation and reduction of Li from its oxide proceeds at voltage > 2 V, which were not used in our cycling tests.

Therefore, in our case,  $\text{Li}_2\text{O}$  was an irreversible phase. A decrease of the capacity was observed in the electrode with a further increase in the annealing temperature of nickel-containing samples. The horizontal plateau typical for silicon lithiation dropped out from the charge profile. Shift of the charge curve was observed towards lower voltages. The values of the capacities of the first cycle and the Coulombic efficiency (CE) are presented in Table 1. The table shows that the decrease in the capacity of Ni-containing electrodes annealed at 800 °C and 1100 °C was accompanied by a decrease in their CE from 52.5 to 26.3%, while for the 600 °C Ni-containing sample, CE retained a value close to the as carbonized sample along with an increase in capacity.

**Table 1.** Values of capacity, Coulombic efficiency of the first cycle and drop of capacity with increasing current density ( $j$ ) after 10 cycles.

No.	$Q_{\text{ch}}$ , mAh/g	$Q_{\text{dch}}$ , mAh/g	Efficiency, %	$\Delta Q_{50\text{mA/g}}/Q_{25\text{mA/g}}$ , %	$\Delta Q_{100\text{mA/g}}/Q_{25\text{mA/g}}$ , %
as carbonized	1290.8	677.7	52.5	10	23
600 °C Ni	1532.3	832.7	54.3	6	17
800 °C Ni	814.5	275.9	33.9	16	36
1100 °C Ni	405.1	106.4	26.3	-	-

The CE increased on subsequent cycles and became constant at 98% (Figure 12a). An increase in the current density ( $j$ ) of the charge/discharge from 25 to 50 and 100 mA/g led to a drop in the capacity of the electrodes, as shown in Figure 12b. Table 1 shows the drop in capacity relative to the capacity at  $j = 25 \text{ mA/g}$ :  $\Delta Q_{50\text{mA/g}}/Q_{25\text{mA/g}} = (Q_{25} - Q_{50})/Q_{25}$  and  $\Delta Q_{100\text{mA/g}}/Q_{25\text{mA/g}} = (Q_{25} - Q_{100})/Q_{25}$ . Therefore, the best rate capability was demonstrated by the Ni-containing anode treated at 600 °C.

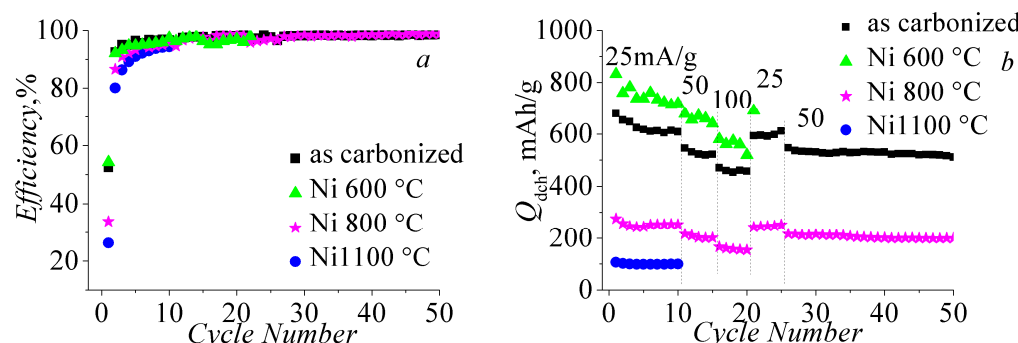


**Figure 12.** Coulombic efficiency (a) and discharge capacity at different currents on the cycle number for as carbonized and nickel-containing electrodes (b).

Improvement of the electrochemical performances of Si-C electrodes by saturation of this material by solution of nickel salt and subsequent annealing at  $T \leq 600$  °C and a sharp degradation at  $T > 600$  °C was due to the different composition of the material. The presence of nickel in the composite apparently leads to an improvement in the electronic conductivity of the composites. As a result, an increase in the capacity and rate capability of the 600 °C Ni electrode was observed compared to the as carbonized electrode. Similar effect was also registered in [30]. The decrease in capacity and rate capability with an increase in the annealing temperature of nickel-containing samples at  $T > 600$  °C were due to the formation of phases of nickel silicides and  $\beta$ -SiC. Consequently, the amount of silicon and carbon, which determine the capacitance and conductivity, decreased.

#### 4. Conclusions

In this work, it was shown that Ni introduced into the Si-C composite was actually capable of increasing the degree of graphitization of carbon. However, its catalytic effect was also found to enhance the reaction on formation of silicon carbide. As a result, heat

treatment of Ni-containing composites already at temperatures of about 800 °C led to a sharp decrease in the concentration of silicon, which is responsible for electrode capacity. Thus, the positive effect of Ni on the structure of the carbon component of Si-C composites was completely eliminated by the formation of SiC and  $\text{Ni}_x\text{Si}_y$ , which led to a decrease in the capacity and rate capability of the electrodes.

**Author Contributions:** Conceptualization, D.A.L. and V.P.U.; Investigation, D.A.L., M.E.K. and A.M.R.; Resources, I.S.K. and A.A.K.; Data Curation, D.A.L. and E.V.A.; Writing—Original Draft Preparation, D.A.L. and E.V.A.; Writing—Review & Editing, V.P.U., D.A.L., E.V.A. and A.A.K.; Project Administration, E.V.A. All authors have read and agreed to the published version of the manuscript.

**Funding:** This research was funded by the State Task 0040-2019-0012.

**Institutional Review Board Statement:** Not applicable.

**Informed Consent Statement:** Not applicable.

**Data Availability Statement:** Not applicable.

**Acknowledgments:** The authors thank A.N. Smirnov for help in analyzing the Raman spectra and Yu.M. Koshtyal for helpful discussions.

**Conflicts of Interest:** The authors declare no conflict of interest.

## References

- Manj, R.Z.A.; Zhang, F.; Rehman, W.U.; Luo, W.; Yang, J. Toward understanding the interaction within Silicon-based anodes for stable lithium storage. *Chem. Eng. J.* **2020**, *385*, 123821. [[CrossRef](#)]
- Obravac, M.N. Review Article Si-alloy negative electrodes for Li-ion batteries. *Curr. Opin. Electrochem.* **2018**, *9*, 8–17. [[CrossRef](#)]
- Li, P.; Kim, H.; Myung, S.-T.; Sun, Y.-K. Diverting Exploration of Silicon Anode into Practical Way: A Review Focused on Silicon–Graphite Composite for Lithium Ion Batteries. *Energy Storage Mater.* **2021**, *35*, 550–576. [[CrossRef](#)]
- Du, F.-H.; Wang, K.-X.; Chen, J.-S. Strategies to succeed in improving the lithium-ion storage properties of silicon nanomaterials. *J. Mater. Chem. A* **2016**, *4*, 32–50. [[CrossRef](#)]
- Xu, Z.-L.; Liu, X.; Luo, Y.; Zhou, L.; Kim, J.-K. Nanosilicon anodes for high performance rechargeable batteries. *Prog. Mater. Sci.* **2017**, *90*, 1–44. [[CrossRef](#)]
- Liu, Y.; Zhou, G.; Liu, K.; Cui, Y. Design of Complex Nanomaterials for Energy Storage: Past Success and Future Opportunity. *Acc. Chem. Res.* **2017**, *50*, 2895–2905. [[CrossRef](#)]
- Liu, X.; Zhu, X.; Pan, D. Solutions for the problems of silicon–carbon anode materials for lithium-ion batteries. *R. Soc. Open Sci.* **2018**, *5*, 172370. [[CrossRef](#)]
- Astrova, E.V.; Ulin, V.P.; Parfeneva, A.V.; Voronkov, V.B. Fluorocarbon Carbonization of Nanocrystalline Silicon. *Tech. Phys. Lett.* **2019**, *45*, 664–667. [[CrossRef](#)]
- Astrova, E.; Ulin, V.; Parfeneva, A.; Rumyantsev, A.; Voronkov, V.; Nashchekin, A.; Nevedomskiy, V.; Koshtyal, Y.; Tomkovich, M. Silicon–carbon nanocomposites produced by reduction of carbon monofluoride by silicon. *J. Alloys Compd.* **2020**, *826*, 154242. [[CrossRef](#)]
- Lozhkina, D.A.; Astrova, E.V.; Likhachev, A.I.; Parfeneva, A.V.; Rumyantsev, A.M.; Smirnov, A.N.; Ulin, V.P. Silicon Monoxide Carbonized by Fluorocarbon As a Composite Material for Anodes of Lithium-Ion Batteries. *Tech. Phys.* **2021**, *66*, 1228–1240. [[CrossRef](#)]
- Yang, Y.; Ren, J.-G.; Wang, X.; Chui, Y.-S.; Wu, Q.-H.; Chen, X.; Zhang, W. Graphene encapsulated and SiC reinforced silicon nanowires as an anode material for lithium ion batteries. *Nanoscale* **2013**, *5*, 8689–8694. [[CrossRef](#)] [[PubMed](#)]
- Ubbelonde, A.R.; Lewis, F.A. *Graphite and Its Crystal Compounds*; Oxford at the Clarendon Press: London, UK, 1960; pp. 9–47.
- Astrova, E.V.; Parfeneva, A.V.; Rumyantsev, A.M.; Ulin, V.P.; Baidakova, M.V.; Nevedomskiy, V.N.; Nashchekin, A.V. The Effect of Thermal Treatment on Properties of Composite Silicon–Carbon Anodes for Lithium-Ion Batteries. *Tech. Phys. Lett.* **2020**, *46*, 114–117. [[CrossRef](#)]
- Sinclair, R.; Itoh, T.; Chin, R. In Situ TEM Studies of Metal–Carbon Reactions. *Microsc. Microanal.* **2002**, *8*, 288–304. [[CrossRef](#)]
- Wang, K.; Cao, Y.; Wang, X.; Kharel, P.R.; Gibbons, W.; Luo, B.; Gu, Z.; Fan, Q.; Metzger, L. Nickel catalytic graphitized porous carbon as electrode material for high performance supercapacitors. *Energy* **2016**, *101*, 9–15. [[CrossRef](#)]
- Thompson, E.; Danks, A.E.; Bourgeois, L.; Schnepf, Z. Iron-catalyzed graphitization of biomass. *Green Chem.* **2015**, *17*, 551–556. [[CrossRef](#)]
- Li, S.S.; Wang, J.K.; Zhu, Q.; Zhao, X.W.; Zhang, H.J. Fabrication of Graphitic Carbon Spheres via a Hydrothermal Carbonization Combined Catalytic Graphitization Method Using Cobalt as Catalysts. *Solid State Phenom.* **2018**, *281*, 807–812. [[CrossRef](#)]
- Wojdyr, M. Fityk: A general-purpose peak fitting program. *J. Appl. Crystallogr.* **2010**, *43*, 1126–1128. [[CrossRef](#)]

19. Gurvich, L.V.; Veits, I.V.; Medvedev, V.A. *Termodinamicheskie Svoistva Individual'nykh Veshchestv*; Nauka: Moscow, Russia, 1978; Volume 1, Book 1. (In Russian)
20. Destyorini, F.; Irmawati, Y.; Hardiansyah, A.; Widodo, H.; Yahya, I.N.D.; Indayaningsih, N.; Yudianti, R.; Hsu, Y.-I.; Uyama, H. Formation of nanostructured graphitic carbon from coconut waste via low-temperature catalytic graphitisation. *Eng. Sci. Technol. Int. J.* **2020**, *24*, 514–523. [[CrossRef](#)]
21. Nakashima, S.; Harima, H. Raman Investigation of SiC Polytypes. *Phys. Stat. Sol. (A)* **1997**, *162*, 39–64. [[CrossRef](#)]
22. Qiang, X.; Li, H.; Zhang, Y.; Tian, S.; Wei, J. Synthesis and Raman scattering of SiC nanowires decorated with SiC polycrystalline nanoparticles. *Mater. Lett.* **2013**, *107*, 315–317. [[CrossRef](#)]
23. Ferrari, A.C.; Robertson, J. Interpretation of Raman spectra of disordered and amorphous carbon. *Phys. Rev. B* **2000**, *61*, 14095. [[CrossRef](#)]
24. Merlen, A.; Buijnsters, J.G.; Pardanaud, C. A Guide to and Review of the Use of Multiwavelength Raman Spectroscopy for Characterizing Defective Aromatic Carbon Solids: From Graphene to Amorphous Carbons. *Coatings* **2017**, *7*, 153. [[CrossRef](#)]
25. Vinogradov, A.Y.; Grudinkin, S.A.; Besedina, N.A.; Koniakhin, S.V.; Rabchinskii, M.K.; Eidelman, E.D.; Golubev, V.G. Structure and Properties of Thin Graphite-Like Films Produced by Magnetron-Assisted Sputtering. *Semiconductors* **2018**, *52*, 914–920. [[CrossRef](#)]
26. Maslova, O.A.; Ammar, M.R.; Guimbretière, G.; Rouzaud, J.-N.; Simon, P. Determination of crystallite size in polished graphitized carbon by Raman spectroscopy. *Phys. Rev. B* **2012**, *86*, 134205. [[CrossRef](#)]
27. Oh, J.H.; Jo, M.S.; Jeong, S.M.; Cho, C.; Kang, Y.C.; Cho, J.S. New synthesis strategy for hollow NiO nanofibers with interstitial nanovoids prepared via electrospinning using camphene for anodes of lithium-ion batteries. *J. Ind. Eng. Chem.* **2019**, *77*, 76–82. [[CrossRef](#)]
28. Wu, D.; Zhao, W.; Wu, H.; Chen, Z.; Li, H.; Zhang, L.Y. Holey graphene confined hollow nickel oxide nanocrystals for lithium ion storage. *Scr. Mater.* **2020**, *178*, 187–192. [[CrossRef](#)]
29. Zhang, X.; Huang, Q.; Zhang, M.; Li, M.; Hu, J.; Yuan, G. Pine wood-derived hollow carbon fibers@NiO@rGO hybrids as sustainable anodes for lithium-ion batteries. *J. Alloys Compd.* **2020**, *822*, 153718. [[CrossRef](#)]
30. Chen, Z.; Ye, J.; Qin, R.; Hao, Q.; Xu, C.; Hou, J. Carbon particles modified macroporous Si/Ni composite as an advanced anode material for lithium ion batteries. *Int. J. Hydrogen Energy* **2019**, *44*, 1078–1087. [[CrossRef](#)]